1

Supplementary Information for

The Entropic Bond in Colloidal Crystals

Eric S. Harper, Greg van Anders, Sharon C. Glotzer

Sharon C. Glotzer.

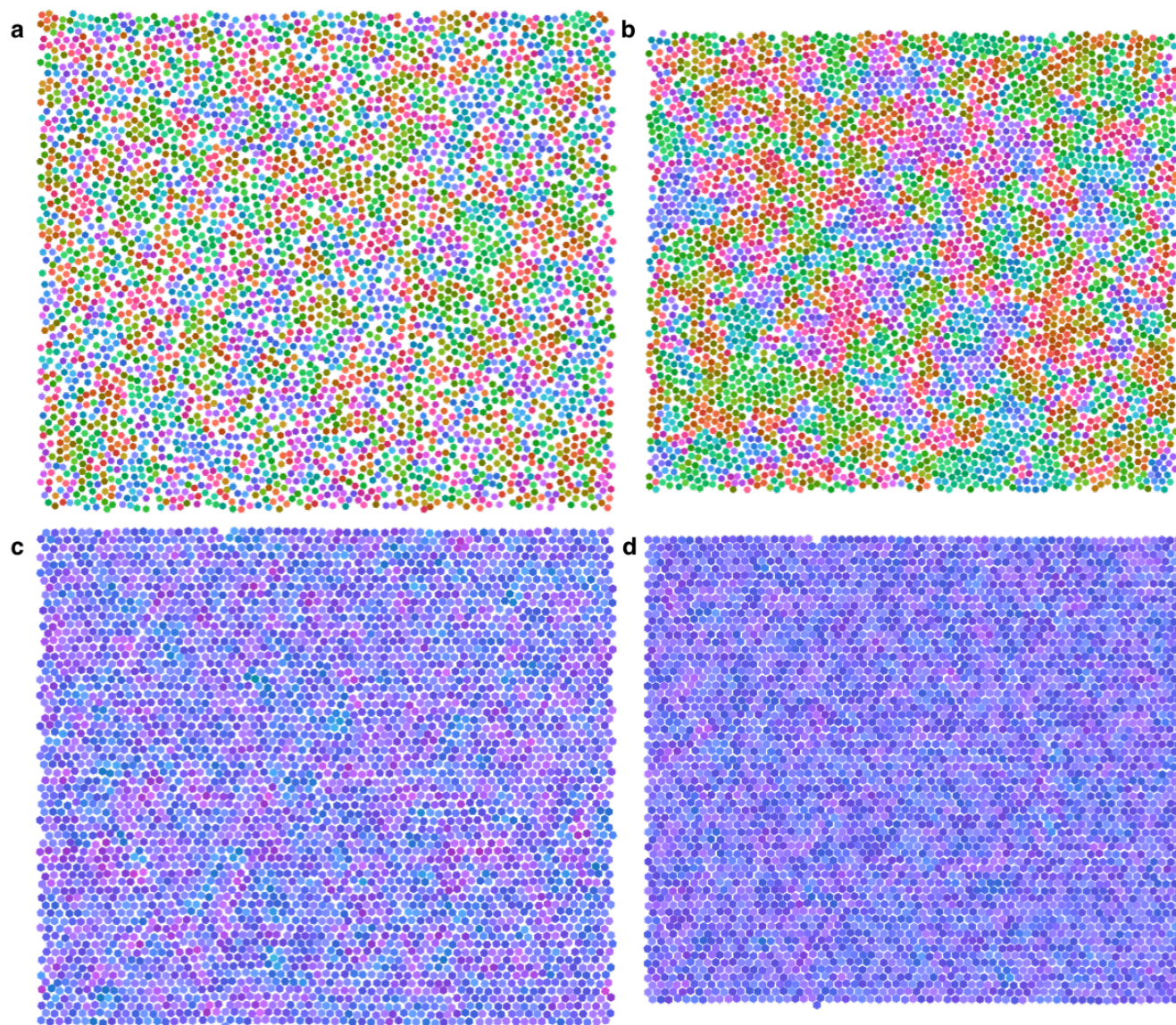**E-mail: sglotzer@umich.edu**

This PDF file includes:

Supplementary text

Figs. S1 to S8

References for SI reference citations

Supporting Information Text

Initialization Procedure and Simulation

Fig. S1. Systems of $N = 4096$ hard hexagons simulated in the *NVT* ensemble at densities **a** $\phi = 0.55$, **b** $\phi = 0.65$, **c** $\phi = 0.75$, and **d** $\phi = 0.85$. Individual polygons are colored by the orientation of their hexatic order parameter, ψ_6(1, 2). This coloration allows for visual identification of different phases: the fluid phase (**a**, **b**) is characterized by a lack of orientational order, while the ordered solid phase (**c**, **d**) is characterized by the presence of orientational order. The difference in these phases is observed by comparing the colors present in the trajectory snapshots. The relatively monochromatic color of the solid phase (**c**, **d**) indicates the long-range hexatic order, while the multiple colors present in the fluid phase (**a**, **b**) indicate the lack of long-range orientational order in the system.

13 Example snapshots of HOOMD-Blue(3–6) simulation trajectories for hard regular hexagons (Fig. S1) and hard elongated
14 hexagons (Fig. S2) in the states in which PMFTs and bond lifetime distributions were computed.

Bond Identification

16 As shown in Fig. S3, the raw PMFT is analyzed to produce a mapping of each discrete geometric configuration to a unique
17 bond. This mapping may then be used to render individual bonds, or track particle geometry during a simulation to compute
18 bond lifetime distributions. Though watershed image segmentation is capable of automatically segmenting the image into
19 different regions (bonds), the scikit-image implementation(9) used is most robust when given the approximate locations of the
20 minima as determined by the lattice positions of the hard hexagons/elongated hexagons Figs. S3,S4,S5,S6.

Eric S. Harper, Greg van Anders, Sharon C. Glotzer
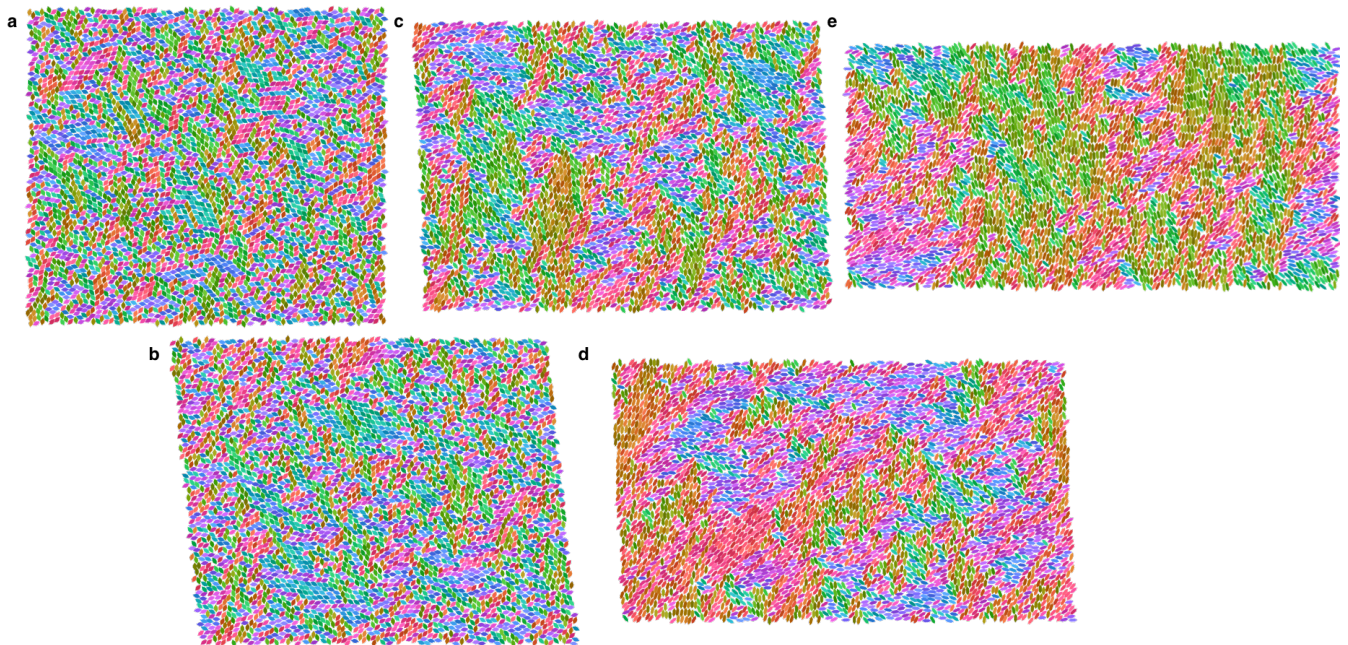
Fig. S2. Systems of $N = 4096$ hard elongated hexagons simulated in the *NPT* ensemble at pressures **a** $P = 16.0$, **b** $P = 14.9$, **c** $P = 13.5$, **d** $P = 12.6$, and **e** $P = 12.1$. Individual polygons are colored by their orientation, taking their two-fold symmetry into account. In contrast to S1, all snapshots show a fluid phase lacking in long-range order, indicated by the presence of all orientations (multiple colors); any orientational order persists over very short distances.
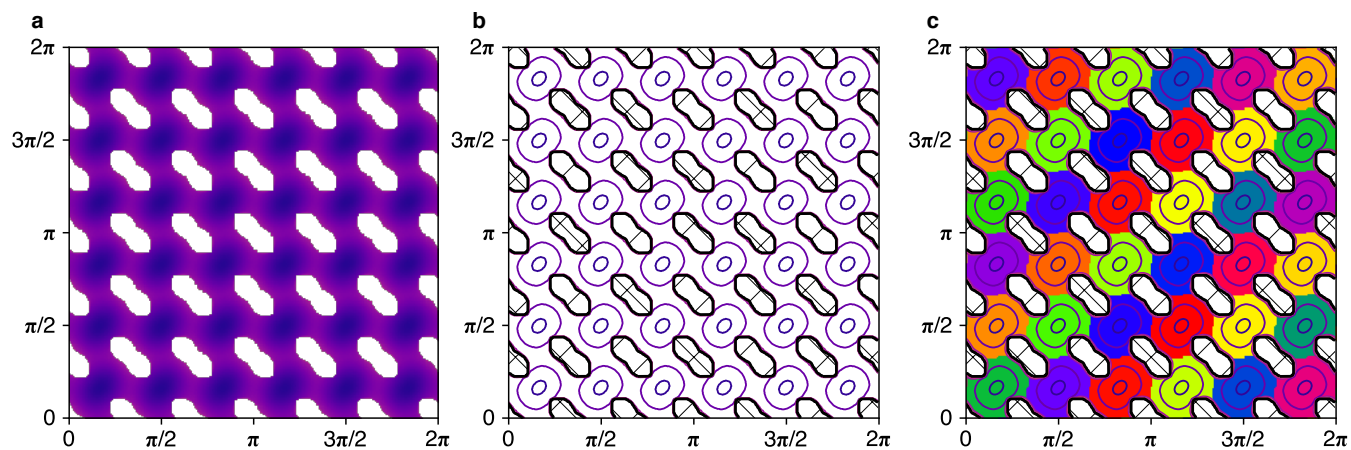
Fig. S3. Summary of the entropic bond analysis pipeline: **a** The raw PMFT is passed through a Gaussian blur **b** (rendered here as contours) to remove any noise or artifacts before passing into the image segmentation algorithm **c**. The full range of the PMFT is shown: $\theta_1, \theta_2 \in [0, 2\pi]$, showing the 36 identical entropic bonds in systems of regular hexagons. Due to the periodic nature of these PMFTs, all other PMFTs shown in this work (both the main text and the SI) display only a single period e.g. $\theta_1, \theta_2 \in \left[0, \frac{\pi}{3}\right]$ for regular hexagons.

Eric S. Harper, Greg van Anders, Sharon C. Glotzer
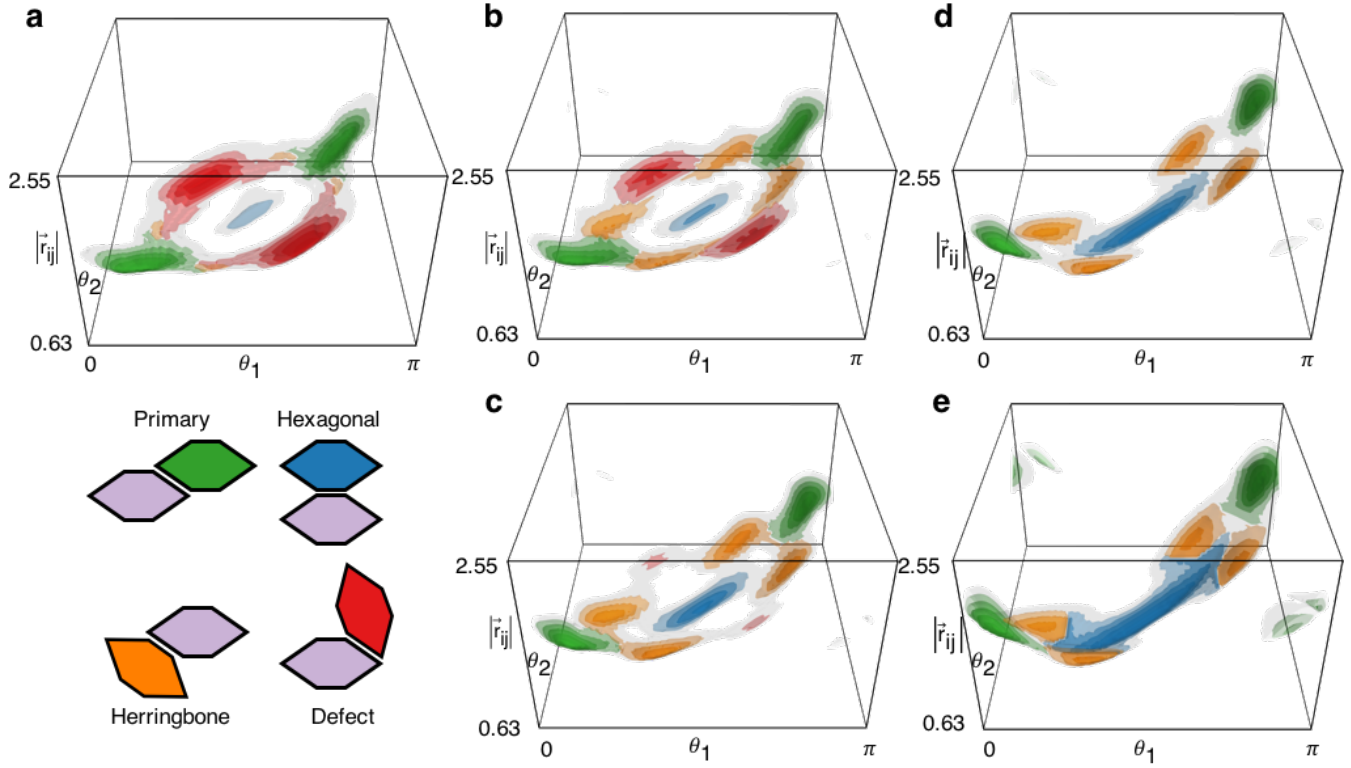
Fig. S4. Isosurfaces of entropically favorable configurations of elongated hexagons, colored by bond (schematic of bonds included to aid in understanding these entropy landscapes) for **a** $\gamma = \frac{1}{2}$, **b** $\gamma = \frac{2}{3}$, **c** $\gamma = 1$, **d** $\gamma = \frac{3}{2}$, and **e** $\gamma = 2$ at pressures $P = [16.0, 14.9, 13.5, 12.6, 12.1]$, respectively. Due to the symmetry of elongated hexagons the entropy landscape is periodic, repeating every π; thus the range of the landscapes is restricted to $\theta_1, \theta_2 \in [0, \pi]$. Excess entropy isosurfaces indicate regions corresponding to each bond type (isosurfaces corresponding to $\Delta S/k_B = [2.5, 2, 1.5, 1, 0.5]$ shown in lighter coloring). $\Delta S = 0$ is indicated with a gray isosurface for reference. The dimensions of the box are set to include the simplest symmetry ($\theta_1, \theta_2 : [0, \pi]$), while the range for values of $|\vec{r_{ij}}|$ is set to the closest approach for all shapes considered ($|\vec{r_{ij}}| = 0.63$) and the farthest distance for which an entropic bond corresponding to a nearest neighbors position for any of the shapes considered ($|\vec{r_{ij}}| = 2.55$).

22   We plot the PMFT as local entropy landscapes for $\gamma = \frac{1}{2}$, $\gamma = \frac{2}{3}$, $\gamma = 1$, $\gamma = \frac{3}{2}$, and $\gamma = 2$ at pressures $P =$
23    $[16.0, 14.9, 13.5, 12.6, 12.1]$, respectively. We include plots of excess entropy density isosurfaces (Fig. S4) with isosurfaces at
24    $\Delta S/k_B = [2.5, 2, 1.5, 1, 0.5]$ shown in lighter coloring) and a gray isosurface at $\Delta S/k_B$ for reference. We also show plots of
25   boundary surfaces between entropic bonds (Figs. S6, S5). Regions belonging to an entropic bonding motif are colored by the
26   motif (see Fig. S8 for motif colors). Both isometric and orthographic views are provided to aid in visual understanding of the
27   regions belonging to each entropic bonding motif.

Disconnectivity Graphs

29   For systems of hard hexagons, the increase in the relative entropy penalty (deepening of the free-energy ''wells") associated
30   with entropic bonds (first nearest neighbors) is a result of the strengthening of the emergent directional entropic force, and
31   should result in longer bond lifetimes at higher densities, shown in Fig. S7. The very high entropy penalty between first and
32   second nearest neighbors at $\phi = 0.75$ indicates that almost all bond breaking should be a result of individual particle rotations,
33   and rarely from first-to-second neighbor exchange.

Interaction Bias

35   To determine the interaction bias required to produce a herringbone lattice over a hexagonal lattice(13), we determine the
36   difference in the number and type of bonds present in each lattice: the hexagonal lattice contains 4 primary bonds and 2
37   hexagonal bonds, while the herringbone lattice contains 4 herringbone bonds and 2 primary bonds (see Fig. 4**a** in the main
38   text). Using the entropy for each bonding motif, we set these two quantities equal and find:

39    $$4\Delta S_{\text{primary}} + 2\Delta S_{\text{hexagonal}} = 4\Delta S_{\text{herringbone}} + 2\Delta S_{\text{primary}}.$$

40

41    $$2\Delta S_{\text{primary}} + 2\Delta S_{\text{hexagonal}} = 4\Delta S_{\text{herringbone}}.$$
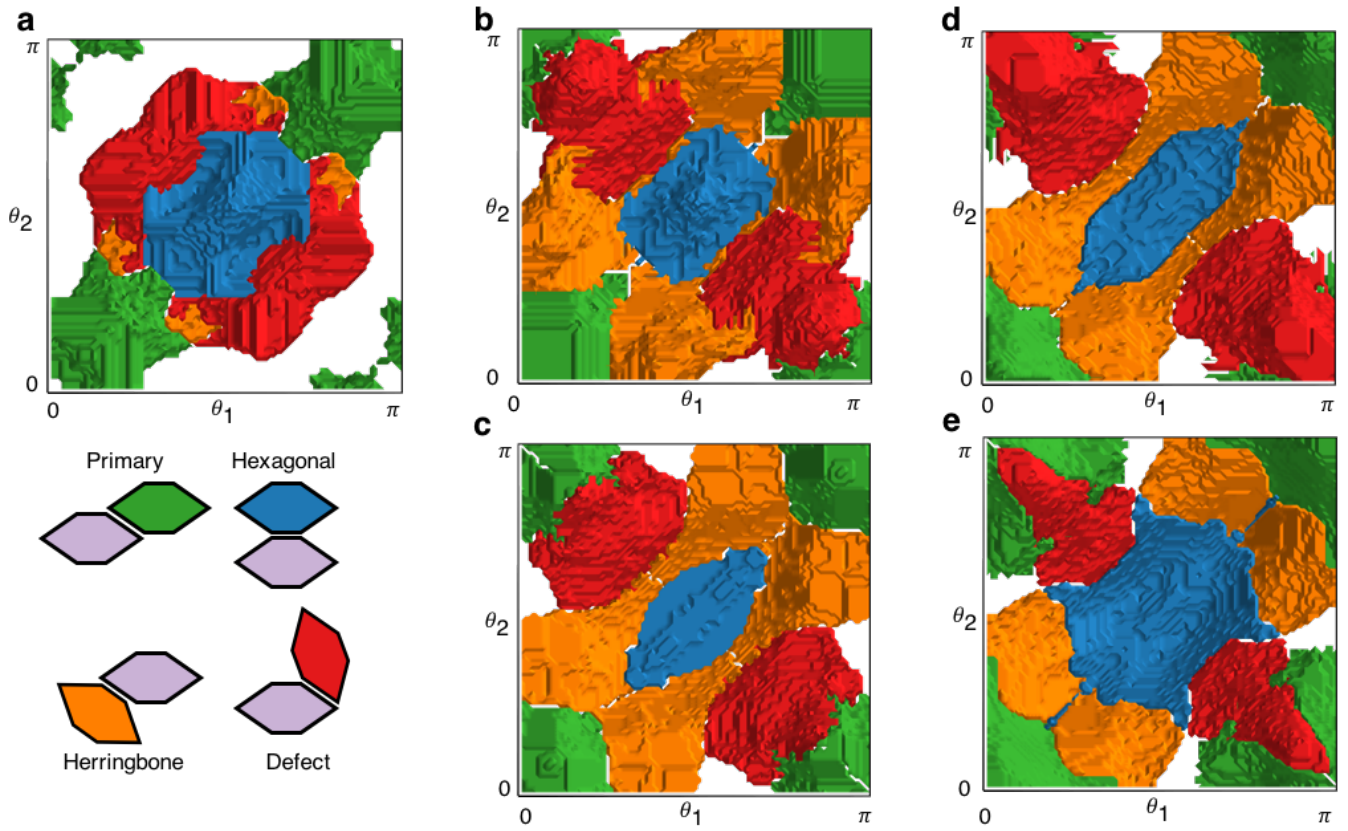
Fig. S5. Orthographic view of the borders of regions belonging to the four different types of bonds in elongated hexagon systems, colored by bond (schematic of bonds included to aid in understanding these entropy landscapes) for **a** $\gamma = \frac{1}{2}$, **b** $\gamma = \frac{2}{3}$, **c** $\gamma = 1$, **d** $\gamma = \frac{3}{2}$, and **e** $\gamma = 2$ at pressures $P = [16.0, 14.9, 13.5, 12.6, 12.1]$, respectively. The size and changes in regions rendered here are analyzed in the alluvial diagram (Fig. 4) in the main text.

**Eric S. Harper, Greg van Anders, Sharon C. Glotzer**
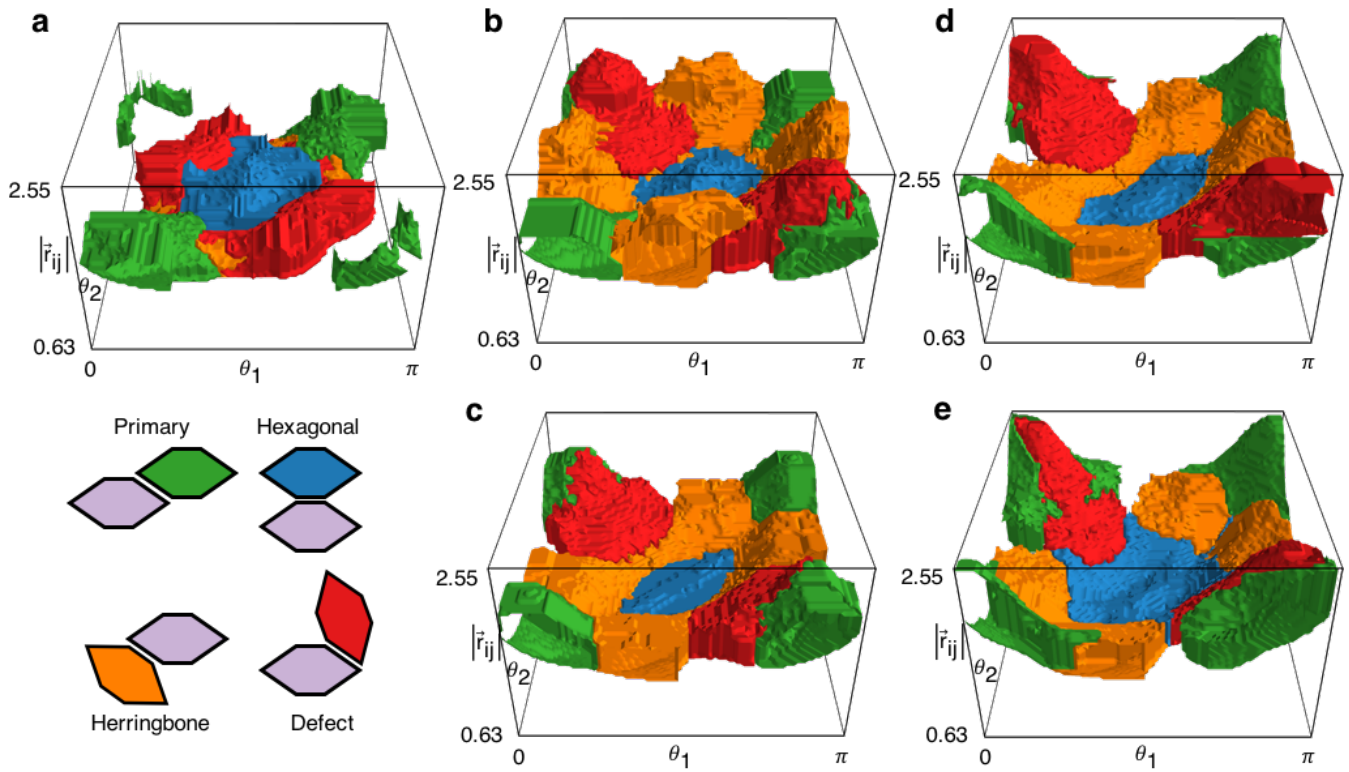
Fig. S6. Borders of regions belonging to the four different types of bonds in elongated hexagon systems, colored by bond (schematic of bonds included to aid in understanding these entropy landscapes) for **a** $\gamma = \frac{1}{2}$, **b** $\gamma = \frac{2}{3}$, **c** $\gamma = 1$, **d** $\gamma = \frac{3}{2}$, and **e** $\gamma = 2$ at pressures $P = [16.0, 14.9, 13.5, 12.6, 12.1]$, respectively. The dimensions of the box are set to include the simplest symmetry ($\theta_1, \theta_2 : [0, \pi]$), while the range for values of $|\vec{r_{ij}}|$ are set to the closest approach for all shapes considered ($|\vec{r_{ij}}| = 0.63$) and the farthest distance for which an entropic bond corresponding to a nearest neighbors position for any of the shapes considered ($|\vec{r_{ij}}| = 2.55$). The size and changes in regions rendered here are analyzed in the alluvial diagram (Fig. 4) in the main text.
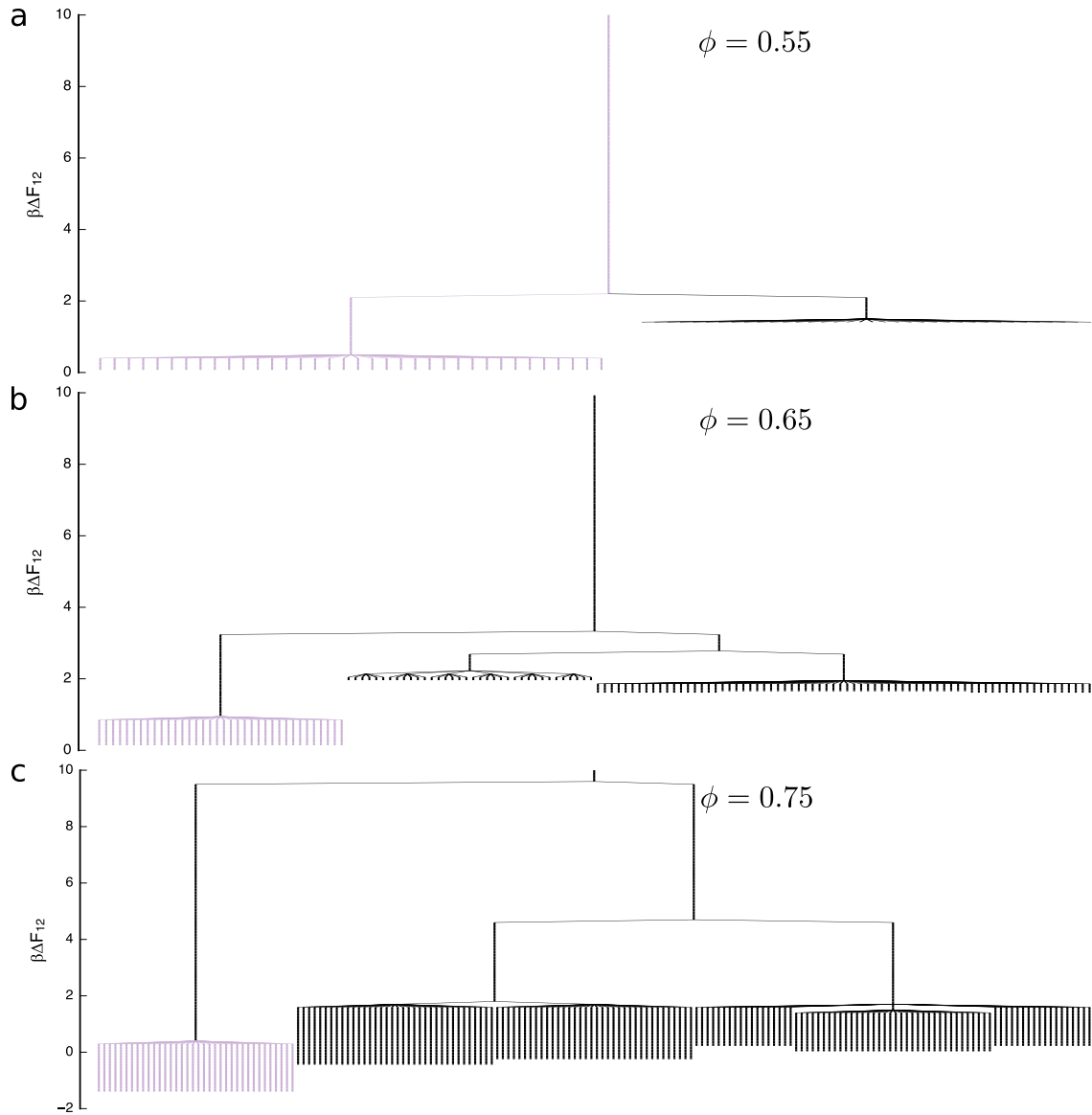
Fig. S7. Disconnectivity graphs plotting $(\beta\Delta F_{12} = -\Delta S/k_B)$ for hard hexagon systems $(\gamma = 0)$ at three different densities. 1st-nearest neighbors are colored purple, while $\geq 2^{nd}$-nearest neighbors are colored black. As density increases, the propensity for particle pairs to align and form entropic bonds increases, as evidenced by a increase in entropy/decrease in free energy. The relative entropy penalty required to break entropic bonds also increases, with an enormous entropy penalty developing in systems at $\phi = 0.75$. The disconnectivity graph for $\phi = 0.85$ is not defined because the entropy penalty between 1st and 2nd-nearest neighbors is infinite.

Eric S. Harper, Greg van Anders, Sharon C. Glotzer
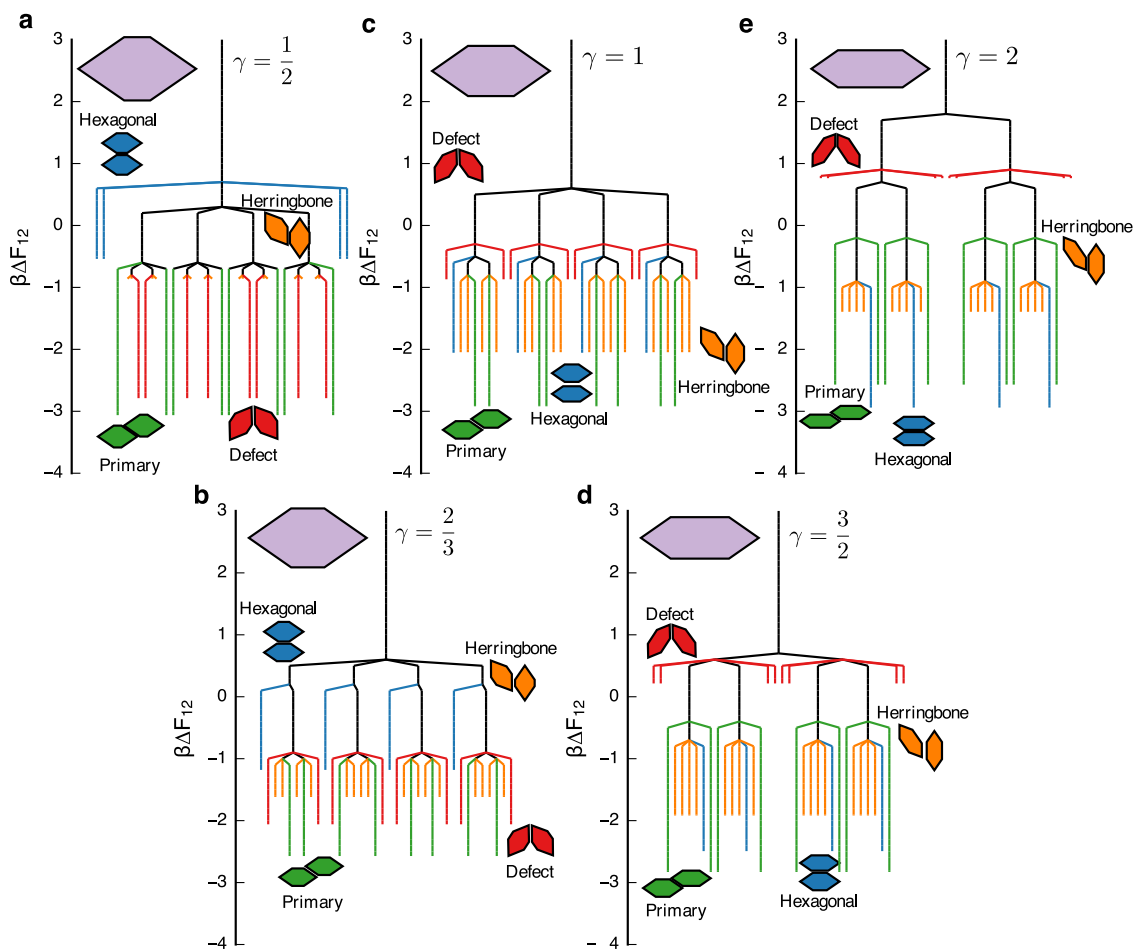
Fig. S8. Disconnectivity graphs plotting ($\beta \Delta F_{12} = -\Delta S/k_B$) showing the entropy maxima/free-energy minima and transition-state entropy for **a** $\gamma = \frac{1}{2}$, **b** $\gamma = \frac{2}{3}$, **c** $\gamma = 1$, **d** $\gamma = \frac{3}{2}$, and **e** $\gamma = 2$. Each leaf represents an entropic bonding motif found at the maxima of the entropy/minima of the free-energy landscape, while each node is the entropy of the meta-basin connecting leaves or nodes. Each line is colored by its corresponding bonding motif. While the herringbone bond has a higher entropy than the hexagonal bond for $\gamma \leq 1$, the herringbone lattice is never observed in entropy-driven self-assembly, leading to the conclusion that the entropy difference is not the determining factor in lattice formation. Rather, for every γ, the relative depth of the hexagonal bond, which corresponds to the entropy penalty required to break a hexagonal bond, is greater than that of the herringbone bond, leading the hexagonal bond to be more stable. Thus, the combination of bond entropy and the relative entropy penalty required to break a bond lead to the preference for hexagonal bonds over herringbone bonds, and the consequent entropy-driven self-assembly of the hexagonal lattice.

Thus, as described in Ref. (13), the interaction bias is the net of breaking two primary bonds and two hexagonal bonds, while forming four herringbone bonds:

$$\beta \Delta S_{12} = (2\Delta S_{\text{primary}} + 2\Delta S_{\text{hexagonal}}) - 4\Delta S_{\text{herringbone}}.$$

By adding a factor to bias the interactions, we can then solve for the bias that makes the interactions equal:

$$0 = (1 + \epsilon)(2\Delta S_{\text{primary}} + 2\Delta S_{\text{hexagonal}}) = 4\Delta S_{\text{herringbone}}.$$

$$(1 + \epsilon) = \frac{(2\Delta S_{\text{primary}} + 2\Delta S_{\text{hexagonal}})}{4\Delta S_{\text{herringbone}}}.$$

References

1. Engel, M., Anderson, J. A., Glotzer, S. C., Isobe, M., Bernard, E. P., & Krauth, W. Hard-disk equation of state: First-order liquid-hexatic transition in two dimensions with three simulation methods. *Phys. Rev. E* **87**, 042134 (2013).

2. Anderson, J. A., Antonaglia, J., Millan, J. A., Engel, M. & Glotzer, S. C. Shape and symmetry determine two-dimensional melting transition of hard polygons. *Physical Review X* **7**, 1–14 (2017). 1606.00687.

3. Anderson, J. A., Lorenz, C. D. & Travesset, A. General purpose molecular dynamics simulations fully implemented on graphics processing units. *J. Comp. Phys.* **227**, 5342 – 5359 (2008). http://codeblue.umich.edu/hoomd-blue.

4. Hoomd-blue. URL http://codeblue.umich.edu/hoomd-blue.

5. Glaser, J., Nguyen, T. D., Anderson, J. A., Lui, P., Spiga, F., Millan, J. A., Morse, D. C. & Glotzer, S. C. Strong scaling of general-purpose molecular dynamics simulations on GPUs. *Computer Physics Communications* **192**, 97 – 107 (2015).

6. Howard, M. P., Anderson, J. A., Nikoubashman, A., Glotzer, S. C. & Panagiotopoulos, A. Z. Efficient neighbor list calculation for molecular simulation of colloidal systems using graphics processing units. *Computer Physics Communications* **203**, 45 – 52 (2016).

7. Anderson, J. A., Irrgang, M. E. & Glotzer, S. C. Scalable metropolis monte carlo for simulation of hard shapes. *Computer Physics Communications* **204**, 21 – 30 (2016). URL http://www.sciencedirect.com/science/article/pii/S001046551630039X.

8. Cousty, J., Bertrand, G., Najman, L. & Couprie, M. Watershed cuts: Minimum spanning forests and the drop of water principle. *Pattern Analysis and Machine Intelligence, IEEE Transactions on* **31**, 1362–1374 (2009).

9. van der Walt, S., Schönberger, J. L., Nunez-Iglesias, J., Boulogne, F., Warner, J. D., Yager, N., Gouillart, E., Yu, T., & the scikit-image contributors scikit-image: image processing in Python. *PeerJ* **2**, e453 (2014).

10. Fichthorn, K. A. & Weinberg, W. H. Theoretical foundations of dynamical monte carlo simulations. *J. Chem. Phys.* **95**, 1090–1096 (1991).

11. Wales, D. *Energy landscapes: Applications to clusters, biomolecules and glasses* (Cambridge University Press, 2003).

12. Smeeton, L. (2016). URL https://github.com/lsmeeton/pyconnect. https://github.com/lsmeeton/pyconnect.

13. Ye, X., Jun, C., Engel, M., Millan, J. A., Li, W., Qi, L., Xing, G., Collins, J. E., Kagan, C. R., Li, J., Glotzer, S. C., & Murray, C .B. Competition of shape and interaction patchiness for self-assembling nanoplates. *Nat. Chem.* **5**, 466–473 (2013).

14. Hunter, J. D. Matplotlib: A 2d graphics environment. *Computing In Science & Engineering* **9**, 90–95 (2007).

15. Ramachandran, P. & Varoquaux, G. Mayavi: 3D Visualization of Scientific Data. *Computing in Science & Engineering* **13**, 40–51 (2011).

16. Teller, S. *Data Visualization with D3.Js* (Packt Publishing, 2013).

17. Bostock, M., Ogievetsky, V. & Heer, J. D3: Data-driven documents. *IEEE Trans. Visualization & Comp. Graphics (Proc. InfoVis)* (2011). URL http://vis.stanford.edu/papers/d3.

18. Freud. URL https://bitbucket.org/glotzer/freud.

19. Jones, E., Oliphant, T., Peterson, P. & others SciPy: Open source scientific tools for Python (2001). URL http://www.scipy.org/. [Online; accessed 2016-09-28].

20. Oliphant, T. E. Python for scientific computing. *Computing in Science & Engineering* **9**, 10 – 20 (2007).

21. Millman, K. J. & Aivazis, M. Python for scientists and engineers. *Computing in Science & Engineering* **13**, 9 – 12 (2011).

22. van der Walt, S., Colbert, S. C. & Varoquaux, G. The numpy array: A structure for efficient numerical computation. *Computing in Science & Engineering* **13**, 22 – 30 (2011).

23. Pérez, F. & Granger, B. E. IPython: a system for interactive scientific computing. *Computing in Science and Engineering* **9**, 21–29 (2007). URL http://ipython.org.